metals

MDPI

Review

Structural Dynamics of Materials under Shock Compression Investigated with Synchrotron Radiation

Kouhei Ichiyanagi [1] and Kazutaka G. Nakamura [2,*]

Received: 30 September 2015; Accepted: 9 December 2015; Published: 15 January 2016
Academic Editor: Klaus-Dieter Liss

[1] Photon Factory, High Energy Accelerator Research Organization, 1-1 Oho, Tsukuba 305-8555, Japan; kouhei.ichiyanagi@kek.jp
[2] Materials and Structures Laboratory, Tokyo Institute of Technology, 4259 Nagatsuta, Yokohama 226-8503, Japan
* Correspondence: nakamura@msl.titech.ac.jp; Tel: +81-45-924-5397; Fax: +81-45-924-5339

Abstract: Characterizing material dynamics in non-equilibrium states is a current challenge in material and physical sciences. Combining laser and X-ray pulse sources enables the material dynamics in non-equilibrium conditions to be directly monitored. In this article, we review our nanosecond time-resolved X-ray diffraction studies with 100-ps X-ray pulses from synchrotron radiation concerning the dynamics of structural phase transitions in non-equilibrium high-pressure conditions induced by laser shock compression. The time evolution of structural deformation of single crystals, polycrystals, and glass materials was investigated. In a single crystal of cadmium sulfide, the expected phase transition was not induced within 10 ns at a peak pressure of 3.92 GPa, and an over-compressed structure was formed. In a polycrystalline sample of Y_2O_3 stabilized tetragonal zirconia, reversible phase transitions between tetragonal and monoclinic phases occur within 20 ns under laser-induced compression and release processes at a peak pressure of 9.8 GPa. In polycrystalline bismuth, a sudden transition from Bi-I to Bi-V phase occurs within approximately 5 ns at 11 GPa, and sequential V–III–II–I phase transitions occur within 30 ns during the pressure release process. In fused silica shocked at 3.5 GPa, an intermediate-range structural change in the nonlinear elastic region was observed.

Keywords: structural dynamics; shock compression; time-resolved X-ray diffraction; synchrotron radiation

1. Introduction

All natural phenomena in physical, chemical, and biological systems change with time and occur away from equilibrium. Characterizing and controlling systems far from equilibrium is now recognized as a great challenge in science and engineering [1]. However, the majority of materials science is devoted to characterizing states and functions at equilibrium. Shock compression is one of the techniques to generate non-equilibrium high-pressure states. A sudden increase of pressure induces phase transitions of materials, which may be the way to study the dynamics in non-equilibrium states. Traditional techniques have limitations in investigating phase transitions that are irreversible or associated with negligible volume change from the step feature in Hugoniot curves or particle velocity profiles [2]. Then, the transient non-equilibrium structures cannot be estimated without the aid of static compression results. The duration of shock compression is short, and time-resolved structural detection is required to investigate the dynamics of phase transitions under shock compression. Combining laser and short X-ray pulses enables the transient structures of non-equilibrium states under shock

compression to be monitored [3–13]. Most studies are limited to X-ray diffraction at one moment during shock compression with a single-shot measurement [6,9–11]. To elucidate the dynamics, time evolution of the structural change needs to be monitored. In the last decade, time evolution in the nanosecond time region has been studied at the Photon Factory Advanced Ring (PF-AR), which is a unique facility with a single-bunch operation. It is important to review the nanosecond dynamics under shock compression performed at the PF-AR, because investigation of the phase transition dynamics at much faster times (picoseconds or femtoseconds) using X-ray free electron lasers has recently attracted considerable attention [13–15].

Here, we review time-resolved X-ray diffraction observations of the structural dynamics in materials in non-equilibrium high-pressure states induced by shock compression at the PF-AR [16–19]. Synchrotron radiation was used as the source of the X-ray pulses. The structure of this paper is as follows. In Section 2, we describe the laser shock compression method and the time-resolved X-ray diffraction setup. In Section 3, we describe three examples of structural dynamics: a single crystal (cadmium sulfide) [16], polycrystal (zirconia ceramics and bismuth) [18,19], and glass (silica glass) samples [17].

2. Synchrotron Facility and Experimental Setup

The dynamics of structural phase transitions under high pressure were directly investigated by nanosecond time-resolved X-ray diffraction using laser induced shock compression and 100-ps pulsed X-rays from synchrotron radiation. In this section, we describe the laser shock compression technique, the synchrotron radiation facility, and the time-resolved X-ray diffraction experimental setup.

2.1. Laser Shock Compression

Since the pioneering work of Bridgman [20,21], the properties of materials under high pressure have been extensively investigated not only in materials science but also in geoscience [21,22] and planetary science. There are two ways to generate high pressure: static compression and shock compression. For static compression, a large press machine has long been used to study material properties and synthesize new functional materials. In addition, diamond anvil cells have been developed and extensively used for optical spectroscopy and structural analysis [23,24]. The main benefits of static compression are the ability to maintain high-pressure conditions and the capability of controlling the temperature. However, the pressure is limited by the fracture strength of the press machine. In addition, a reference point obtained by dynamic-compression experiments is required to determine the induced pressure. Conversely, in shock compression, the induced pressure is not limited by the fracture strength of the materials, and the pressure is determined by measuring shock and particle velocities with conservation laws [2]. The materials are compressed to a high-pressure state in a very short time (e.g., nanosecond time scale) by shock compression. The induced state is a non-equilibrium state that reverts to the equilibrium state with time. The dynamics of materials in non-equilibrium high-pressure states can be monitored using appropriate time-resolved measurements.

A conventional technique to generate a shock wave is hypervelocity impact of the target materials with a projectile, which is accelerated using a light-gas gun [25–28]. It is very difficult to synchronize firing gunpowder and triggering electric devices with high time accuracy (e.g., within nanoseconds). In recent times, a high-power laser pulse technique has evolved to induce shock compression via laser ablation, which is called laser-shock compression. Using this technique, it is very easy to synchronize the electronic measurement devices and timing of the shock compression with very high accuracy (nanoseconds) [5,29–33]. In addition, ultrahigh pressures above 1 TPa can be achieved using an intense laser pulse [34–39].

There are two main target geometries for laser-shock compression. One is a direct-irradiation target, which consists of a sample and an ablator (usually aluminum foil). When the laser pulse irradiates the ablator surface, laser ablation occurs. A shock wave induced by reaction to the laser ablation propagates into the sample. The peak pressure of this process can be estimated by the

equation $P \approx 8.6 \times 10^{11}(I/10^{14})^{2/3}\lambda^{-2/3}$, where P is the pressure (Pa), I is the laser power density ($W \cdot cm^{-2}$), and λ is the wavelength (μm) [40]. This direct laser-shock compression is frequently used for very high-power laser irradiation (higher than TW/cm^2). The other target is a plasma-confined target, which has a sandwich structure consisting of the sample, an ablation foil, and a cover layer, which is transparent at the laser wavelength. The laser pulse penetrates the cover layer and induces ablation at the ablator surface, and the ablation plume is confined between the sample and the cover layer. For the cover layer, glass and polymer foils are usually used. In this case, the induced pressure and the shock duration are enhanced. The peak pressure can be estimated with the equation $P \approx 3.16 \times 10^2\sqrt{\alpha/(2\alpha+3)}\sqrt{IZ}$, where P is the pressure (Pa), I is the laser power density ($W \cdot cm^{-2}$), Z is the shock impedance ($g \cdot cm^{-2} \cdot s^{-1}$), and α is a constant [41]. Using the plasma-confined target, much higher pressures than the direct-irradiation target can be generated with the same laser power density. However, there is a limit for the applied power density because of the ablation threshold of the cover layer. The time evolution of the induced pressure can be obtained by measuring the shock and particle velocities [2].

2.2. Time-Resolved X-ray Diffraction Setup

We developed a single-shot time-resolved X-ray diffraction and scattering measurement system based on the storage-ring synchrotron X-ray source at the NW14A beamline of the Photon Factory Advanced Ring (PF-AR) in Tsukuba, Japan [42]. The PF-AR operates in a single-bunch mode at 6.5 GeV electron energy and supplies high-intensity hard X-ray pulses at a repetition rate of 794 kHz. The complete experimental setup of the single-shot time-resolved X-ray measurement system is shown in Figure 1. The pump source for shock wave generation was a Q-switched yttrium aluminum garnet (YAG) laser (Powerlite 8000, Continuum Inc., San Jose, CA, USA). The wavelength, pulse width, and energy were 1.064 μm, 8 ns (full width of half maximum and Gaussian shape), and ~1 J/pulse, respectively. The peak energy and pulse width of the probe X-ray pulse were 15.6 keV and 100 ps, respectively. The energy band width of the X-ray can be changed with the sample condition. We will describe the energy-band width of the X-ray source in more detail later. The frequency of the X-ray pulse train was divided by an X-ray pulse selector (XPS) from 794 kHz–946 Hz. Then, the single X-ray pulse was picked up by the high-speed solenoid X-ray shutter (XRS1, Uniblitz Shutter System, Rochester, NY, USA). The pump laser was synchronized with the frequency of the divided X-ray pulse at 9.46 Hz using a PF master clock of 508 MHz. The 946 Hz X-ray was reduced to 9.46 Hz by a frequency divider [16]. The single laser pulse synchronized with the X-ray pulse was also selected using a solenoid laser shutter. The delay time between the X-ray and laser pulses (Δt) was controlled by a delay generator (DG645, Stanford Research System Inc., Sunnyvale, CA, USA). The timing jitter in this measurement system is about 1 ns. The X-ray diffraction and scattering patterns were recorded on a two-dimensional (2D) charge-coupled device (CCD) detector (MarCCD 165, Rayonix, Evanston, IL, USA) with a diameter of 165 mm. The same CCD detector was used for all of the experiments, and the single-shot images were obtained without accumulation.

The pump-laser and probe X-ray were focused to 0.45×0.45 mm^2 or 0.45×0.25 mm^2 on the ablator surface. The pump-laser was irradiated at about 15°–20° normal to the sample. We carefully aligned both the X-ray and laser beams as follows. First, we checked the X-ray beam position at the sample position using the pinhole scan technique, in which we checked the beam center and beam width by measuring the X-ray intensity through the pinhole by scanning the pinhole position. The pinhole position was also monitored by using a microscope, which was fixed at a certain position. We then placed a fluorescent plate at the sample position. The laser beam was focused on the plate and the fluorescence from the focused spot was monitored by the microscope. The single laser pulse destroyed and removed the sample in the X-ray path. We changed the sample after taking a single scattering image of the shocked sample at each delay time.

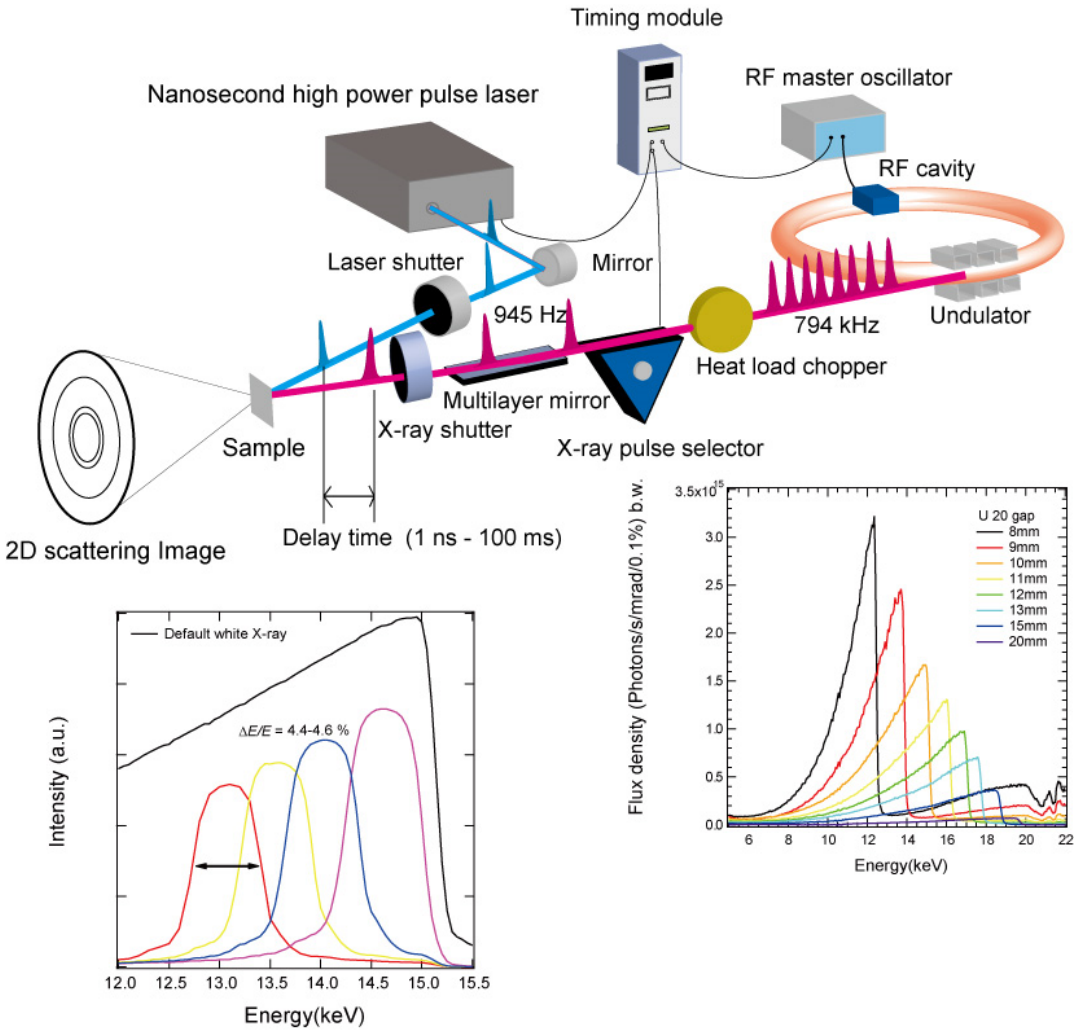

Figure 1. Schematic diagram of the single-shot time-resolved X-ray diffraction and scattering system at beamline NW14A of the PF-AR. The energy bandwidth of the X-ray is changed by the X-ray multilayer optics with the depth graded Ru/C from the default X-ray spectrum to $\Delta E/E$ = 4.4%–4.6%. The pump-laser for shock-wave generation and the X-ray pulse selector and shutter are synchronized with the RF master oscillator. The insert figures show the default X-ray spectrum from the U20 and the Gaussian-shaped and narrow energy bandwidth of the X-ray spectrum using the X-ray multilayer optics, which is modified from Figure 3 in [43].

The energy bandwidth of the probe X-ray was adjusted by the multilayer optics downstream of XPS. The default X-ray energy bandwidth that is suitable for the single-shot Laue diffraction measurement is $\Delta E/E$ = 15% with a broad asymmetric energy spectrum from an undulator with a period length of 20 mm (U20) [42]. The photon flux was 10^9 photons/pulse. However, the broad X-ray energy bandwidth is not suitable for time-resolved X-ray diffraction and scattering measurements of laser-induced shocked polycrystalline and amorphous materials. Therefore, we changed the X-ray energy bandwidth to the sample configuration. A depth-graded Ru/C layer on monocrystalline Si provided a Gaussian-shaped $\Delta E/E$ = 4.4%–4.6% X-ray energy bandwidth from the default undulator X-ray spectrum [43]. This photon flux was 3×10^8 photons/pulse. We can use the discretional energy bandwidth in the X-ray for the spectrum without reducing the photon flux per pulse.

3. Structural Dynamics

3.1. Over-Compressed State in a Single Crystal of Cadmium Sulfide

The shock-induced phase transitions of cadmium sulfide (CdS) have been studied by time-resolved spectroscopy using a light gas gun [44,45]. The wurtzite-rocksalt phase transition has been reported to occur at 2.92 and 3.25 GPa for *a*-axis and *c*-axis compression, respectively [46,47]. The dynamics of the structural phase transition of CdS under shock compression has attracted much attention because an intermediate phase with a face-centered tetragonal structure has been proposed [44]. Using nanosecond time-resolved Laue diffraction and laser shock compression, the structural dynamics of CdS under shock compression at a peak pressure of 3.92 GPa were monitored.

The target assembly had a plasma-confined geometry consisting of three layers: a PET film (25 μm thick), an Al ablator (50 nm thick), and a single crystal of CdS (50 μm thick) [16]. The CdS crystal had a (001) orientation. Laue diffraction was performed with a white X-ray pulse with a peak energy of 16 KeV and an energy width ($\Delta E/E$) of 15%. The photon flux of the X rays was 10^9 phonons/pulse. The 10 ns laser pulse with a wavelength of 1064 nm and energy of 860 mJ was focused on a 0.4 × 0.4 mm^2 spot on the sample. The spot size of the X-ray pulse was 0.49 × 0.24 mm^2, and then a small part of the non-laser-irradiated sample was also probed.

Laue diffraction images under laser-shock compression for typical time delays (0, 6, 12, and 22 ns) are shown in Figure 2. The delay between the laser and X-ray pulses was determined at the sample position with their half maximum intensities. We monitored the timing of the laser and X-ray pulses for each shot using photodiodes set in the optical path. The relative delay when the pulse reached the monitor and the sample position was calibrated. Before laser irradiation, there are diffraction spots with hexagonal symmetry corresponding to the wurtzite structure. Under shock compression, the Laue images retain this hexagonal feature and all of the peaks move to the higher angle side of 2θ and then back to their original positions, which suggest that the laser-induced shock compression is parallel to the *c*-axis direction. The changes of the positions of the 201 and 302 Bragg peaks with time are shown in Figure 3.

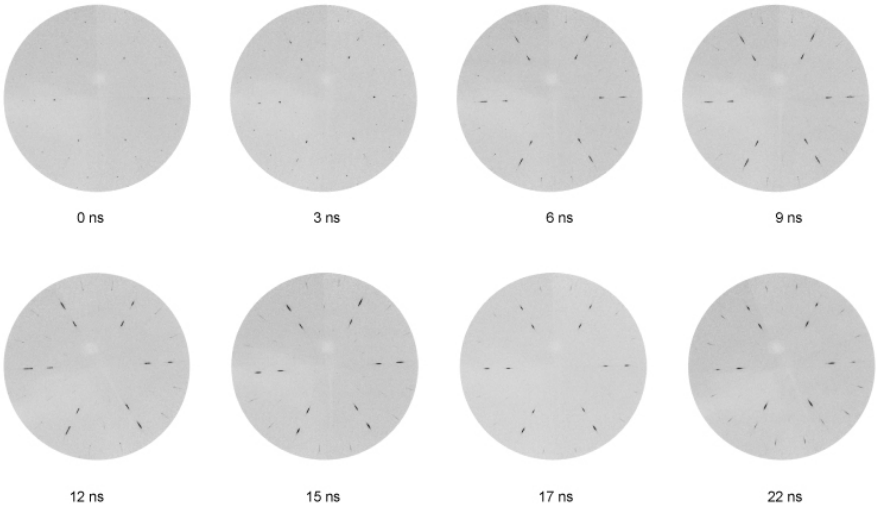

Figure 2. Laue diffraction images of CdS under laser-shock compression at Δt = 0, 6, 12, and 22 ns [16]. Reproduced with permission from [Applied Physics Letters]. Copyright [2007], AIP Publishing LLC.

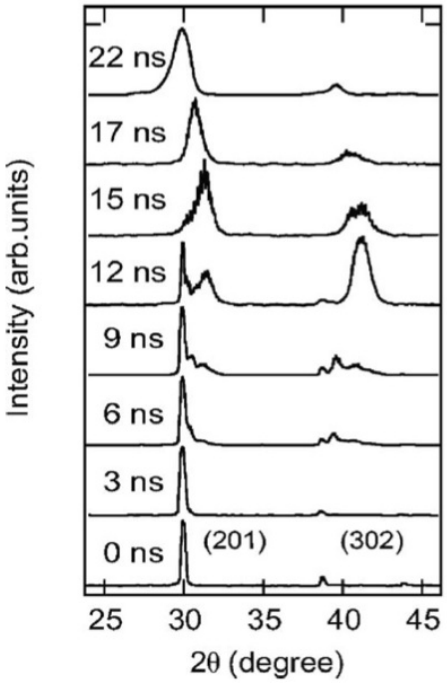

Figure 3. Positions of the 201and 302 Bragg peaks at Δt = 0, 3, 6, 9, 12, 15, 17, and 22 ns [16]. Reproduced with permission from [Applied Physics Letters]. Copyright [2007], AIP Publishing LLC.

The 201 peak intensity decreased after laser irradiation. A higher angle shifted peak appeared and its intensity increased until Δt = 15 ns. For Δt > 17 ns, the new peak shifted to a lower angle. This feature can be explained by laser ablation generating a shock wave, which propagates inside the sample with a shock speed. At a certain time delay, shock-compressed and uncompressed (pristine sample) regions exist inside the sample, and the X-ray diffraction pattern then consists of both the original peak and the higher angle shifted peak from the compressed region. As the delay increases, the shocked volume increases and the intensity of the higher angle shifted peak increases. When the shock front reaches the rear side of the sample, a release wave and shock-wave reflection account for the decreased shock pressure. The peak position then returns to the original position after 22 ns. The shock speed was estimated to be 4.2 $\pm$ 0.5 km/s from the time evolution of the higher angle shifted peak. This value is in good agreement with the previously reported elastic velocity [47]. The maximum compression was estimated to be 4.4% of the cell volume from the 201 peak shift [48]. The shock pressure was estimated to be 3.92 GPa from volume compression, which is higher than the phase transition pressure (3.25 GPa) for the wurtzite-rocksalt phase transition by *c*-axis compression.

Although the shock pressure is higher than the phase transition pressure, the phase transition did not occur within 15 ns under shock compression. This indicates that the shock-induced structural phase transition does not instantaneously occur and requires an incubation time for a single-crystal sample. From another point of view, the over-compressed structure, which is not realized in equilibrium conditions, is generated within nanoseconds in a non-equilibrium high-pressure state.

3.2. Reversible Phase Transition in Zirconia Ceramics

Y_2O_3 (3 mol %) stabilized tetragonal zirconia polycrystalline (3Y-TZP) ceramics are widely used engineering ceramics because of their high strength and toughness [49]. Although the phase diagram of pure zirconia is well established, the phase stability of 3Y-TZP under high pressure is controversial [50–52]. The tetragonal structure transforms to a disordered structure or an orthorhombic II phase via a monoclinic phase under static compression. Tetragonal zirconia directly transforms to the orthorhombic II phase during shock compression or a quenchable monoclinic phase during

the shock release process. The transformation path between the tetragonal and monoclinic phases is not well established. The transient structure under shock compression can only be assessed by time-resolved X-ray diffraction.

The target assembly had a plasma-confined geometry consisting of three layers: a plastic film (25 μm thick), an Al ablation film (1 μm thick), and the 3Y-TZP sample (50 μm thick) [18]. The 3Y-TZP was a polycrystalline sample obtained from Tosoh Co. (Tokyo, Japan). The X-ray pulse used in these experiments had a peak energy of 15.6 KeV, a bandwidth of 4.4%, and a flux of 3×10^8 photons/pulse. The 10 ns laser pulse with a wavelength of 1064 nm and energy of 700 mJ was focused on a 0.4×0.4 mm^2 spot on the sample. The peak pressure in the sample was estimated to be 9.8 GPa.

Figure 4 shows a typical example of the Debye-Scherrer pattern (Figure 4a) and the rocking curves obtained by integrating the Debye-Scherrer ring of 3Y-TZP before laser irradiation (Figure 4b), which clearly shows that the pristine sample had a tetragonal structure. The error of the diffraction intensity was estimated to be approximately 5% from the fluctuation of several signals.

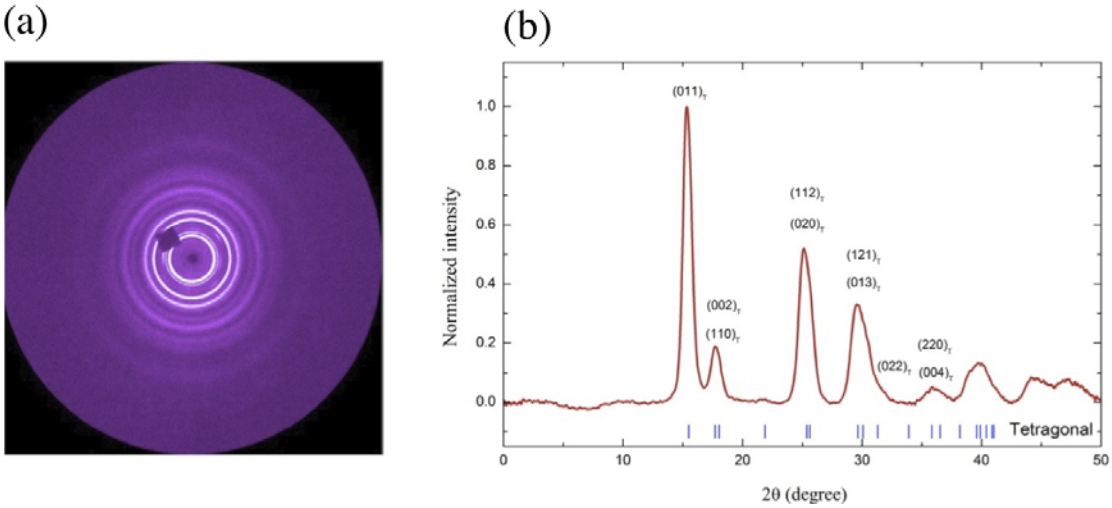

Figure 4. X-ray diffraction of the pristine sample of 3Y-TZP. (**a**) Debye-Scherrer ring detected by a CCD camera. The black square is the shadow of the laser beam block. (**b**) X-ray diffraction intensity profile obtained from the Debye-Scherrer ring. The stick diagram shows the peak positions of the tetragonal phase [18]. Reproduced with permission from [Journal of Applied Physics]. Copyright [2012], AIP Publishing LLC.

Nanosecond time-resolved X-ray diffraction experiments were performed using the pump-probe protocol. X-ray diffraction was performed before and after laser irradiation, and each rocking curve was normalized by its total intensity from $2\theta = 0$–60°. The change is obtained from the differential signals obtained by subtracting the rocking curve obtained after laser irradiation from that before irradiation.

Figure 5 shows the change of the differential signals of the X-ray diffraction intensity profile after laser irradiation for $\Delta t = 5$–1005 ns. For $\Delta t < 25$ ns, diffraction peaks appear at 11°, 13°, and 16°, which correspond to the 110, 1−11, and 111 peaks of the monoclinic phase, respectively. The peak intensity increased with increasing delay for $\Delta t < 15$ ns and then decreased for $\Delta t > 15$ ns. The intensity of the 110 peak of the tetragonal phase increases with increasing delay. In this time range, both the tetragonal and monoclinic phases coexist under shock compression.

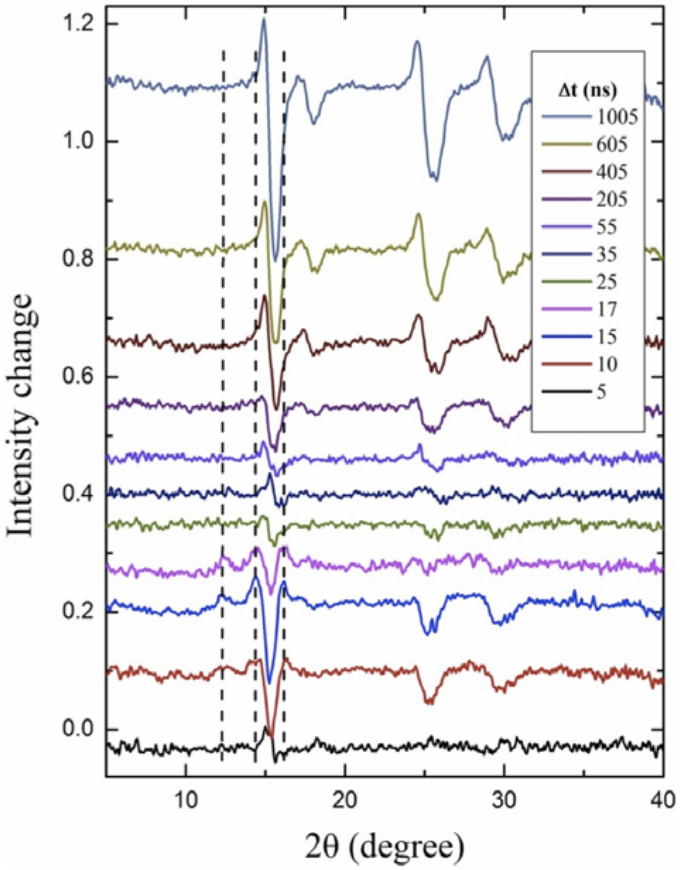

Figure 5. Change of the differential signal of the X-ray diffraction intensity profile from laser-shocked 3Y-TZP with delay time. The dashed lines represent the 110, 1–11 and 111 peak position of the monoclinic phase [18]. Reproduced with permission from [Journal of Applied Physics]. Copyright [2012], AIP Publishing LLC.

For Δt > 55 ns, the differential signal corresponding to the 110 peak of the tetragonal phase at ~15° is positive and negative at lower and higher angles, respectively. This means that the peak shifted to lower angle, indicating volume expansion induced by pressure release. The results clearly indicate that laser-shocked 3Y-TZP ceramics undergo a reversible tetragonal-monoclinic phase transition in a nanosecond time regime under shock compression and release processes, although an irreversible transition has been suggested by previous shock–recovery investigations.

3.3. Phase Transition Dynamics in Polycrystalline Bismuth

Bismuth has one of the most complicated phase diagrams, and its phase transition point is used as a pressure standard for static high-pressure experiments [53–56]. The kinetic process of the Bi-I to Bi-II transition has been extensively investigated, although it has only recently been semi-qualitatively understood through a ramp compression technique. However, information about the structural dynamics of bismuth under shock compression is quite limited. The sequence of shock-induced polymorphous transformations beyond the Bi-I to Bi-II transition has not been systematically identified. Furthermore, the dynamics during the shock release process have been proven to be almost unobtainable, owing to the complexity arising from the quasi-elastic release effect and the release-induced multiple phase transition. Here, we investigated the dynamics of the structural phase transition of bismuth under shock compression of approximately 11 GPa, which is higher than the reported phase transition pressure of 7.7 GPa for the B-V phase [55].

The plasma confined target consisted of a backup plastic film (25 μm thick), an Al foil (3 μm thick), and the sample. The sample was a 20 μm thick foil of polycrystalline bismuth (99.97% pure) obtained from Goodfellow Cambridge Limited (Huntingdon, UK) [19]. A laser pulse with energy of 1.0 J and pulse width of 8 ns was focused on the target with a spot diameter of 0.48 mm. The peak pressure was estimated to be 11 GPa using the Fabbro-Devaux model [41]. The X-ray pulse had energy of 15.6 KeV and a band width of 1.4%. X-ray diffraction showed a Debye-Scherrer ring pattern in a characteristic form of the polycrystal. The X-ray diffraction intensity profile was obtained by azimuthally averaging the Debye-Scherrer diffraction patterns. The X-ray diffraction intensity profile from the pristine sample (at a delay of 0 ns in Figure 6) is in the Bi-I (R−3m) phase. The most intense peak at 14° is the 110 line of the Bi-I phase.

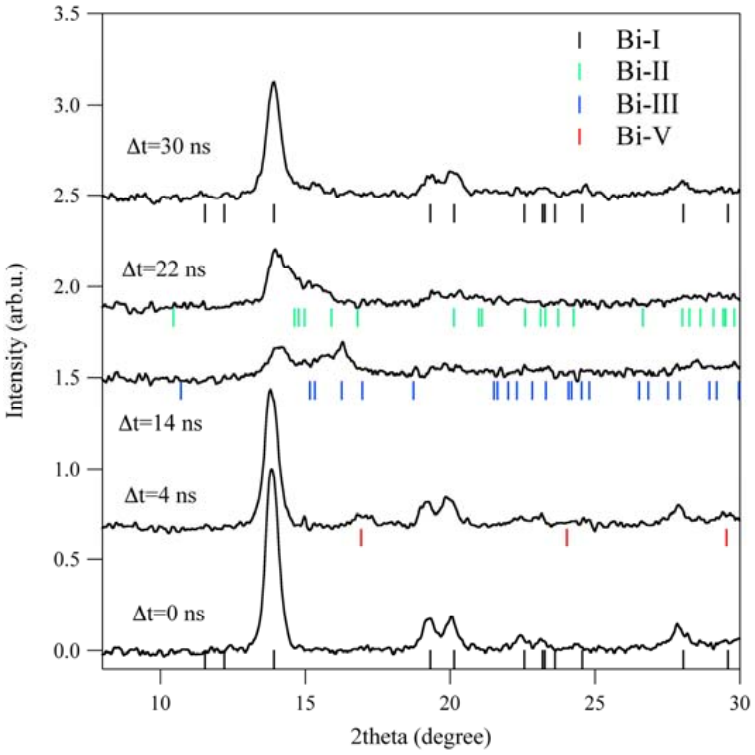

Figure 6. Time evolution of X-ray diffraction intensity profile along of laser-shocked bismuth at Δt = 0, 4, 14, 22, and 30 ns [19]. Reproduced with permission from [Applied Physics Letters]. Copyright [2013], AIP Publishing LLC.

To systematically investigate the structural dynamics after laser irradiation, a series of pump-probe measurements were performed for $-2 \leqslant \Delta t \leqslant 36$ ns. Selected signals at Δt = 0, 4, 14, 20, and 30 ns are shown in Figure 6, and are compared with the calculated diffraction-peak positions of the Bi-I to B-V phases. The new peaks correspond to the Bi-V phase (Im−3m) at 4 ns, the Bi-III phase at Δt = 14 ns, and the Bi-II phase at Δt = 20 ns. At Δt = 30 ns, the shocked sample transformed back to the Bi-I phase. Transient structural information at each delay was extracted by comparing the experimental diffraction profile with the calculated diffraction peaks. The time evolution of the structure is schematically summarized in Figure 7 with a pressure profile estimated using the Fabbro-Devaux model [41] and a Gaussian laser profile. It shows that the Bi-I phase transforms to the Bi-V phase within approximately 5 ns during compression and then sequentially transforms to Bi-III, Bi-II, and Bi-I within 30 ns during the release process.

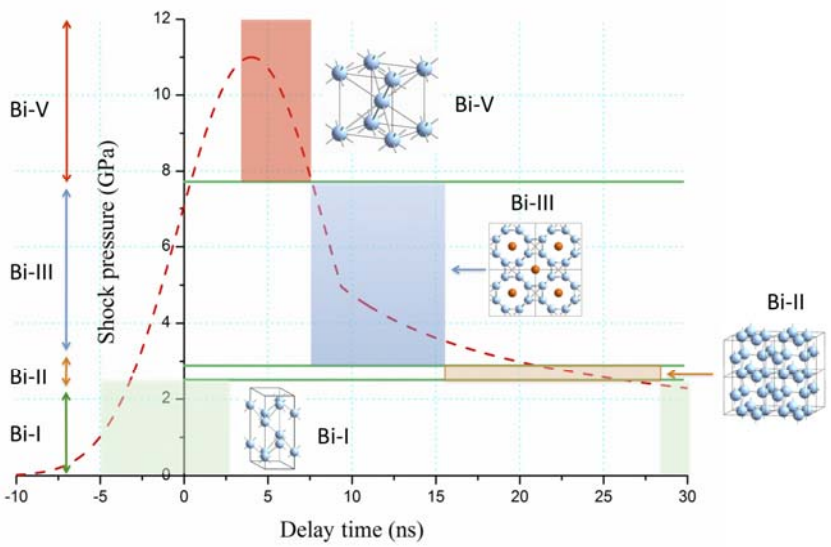

Figure 7. Time evolution of structure of bismuth under laser shock compression [19]. Reproduced with permission from [Applied Physics Letters]. Copyright [2013], AIP Publishing LLC.

The observed transformation from Bi-I to Bi-V appears to be a direct transformation. There are two possibilities. One is that the time the sample spends as the Bi-II and Bi-III phases during compression is too short for to it to be resolved with the current experimental conditions. The other arises from the reconstructive character of the Bi-I to Bi-II transition, which requires an incubation time of tens of nanoseconds. Thus, the Bi-I phase would be over-shocked to the Bi-V phase, although the displacive transformation path between the two phases is still unknown.

Recently, the shock-compression and pressure-release processes of bismuth at shock pressures up to 14 GPa have been investigated using femtoseocond X-ray diffraction with a X-ray free electron laser [13]. The Bi-V phase under compression was also observed. In the pressure-release process from the Bi-V phase, melting was observed within 3 ns. Time-resolved X-ray diffraction is thus an excellent way to determine the nature and time scale of phase transitions induced by shock compression.

3.4. Intermediate Structural Deformation in Shock-Compressed Silica Glass

The response of silica glass to shock compression has been investigated for many years. The behavior of the intermediate- and short-range structures in shock-compressed silica glass is important to understand the shock fracture process. Below 10 GPa, silica glass densification mainly occurs for changes in the intermediate-range structure, as indicated by the first sharp diffraction peak (FSDP) at 1.55 $Å^{-1}$ with a Fourier component period of approximately 4 Å [57]. A nonlinear elastic response below 9 GPa has been observed in many types of silicate glass by free surface velocity measurement. The shock wave front in the elastic shock pressure region produces a non-discontinuous ramp wave front [58,59]. However, the shocked structure of silica glass has not been observed because the X-ray scattering signal using one X-ray pulse is very week. We used a $\Delta E/E$ = 4.6% energy bandwidth of the probe X-ray pulse with a peak energy of 15.6 KeV. We investigated the dynamics of the intermediate-range structure in silica glass under elastic shock-wave loading of around 4 GPa by time-resolved X-ray scattering measurements.

We fabricated the sample assembly with a plasma confined geometry, as shown in Figure 8a. The sample consisted of silica glass, aluminum film, and poly(ethylene terephthalate) (PET) film to confine the plasma [17]. The sample size was 5 × 5 ×70 μm^3 and the thicknesses of aluminum and the PET film were 18 and 25 μm, respectively. The laser ablation was generated at the aluminum-PET film interface, and the shock wave propagated into the aluminum and silica glass. At Δt = 0 ns, the laser intensity at the aluminum surface was 50%. We constructed a one-dimensional radial scattering curve for each

delay time by integrated the 2D X-ray scattering pattern. Figure 8b shows the X-ray scattering patterns as a function of Q, where $Q = (4\pi/\lambda)\sin\theta$, before laser irradiation and at Δt = 10 ns with the X-ray scattering silica glass and aluminum film peaks labeled. We estimated the shock pressure of silica glass by the impedance matching method using the shift of the 111 aluminum diffraction peak and the compressive data of silica glass in the nonlinear elastic shock region [60,61]. The mean maximum shock pressure in silica glass was estimated to be 3.5 GPa by the impedance matching method.

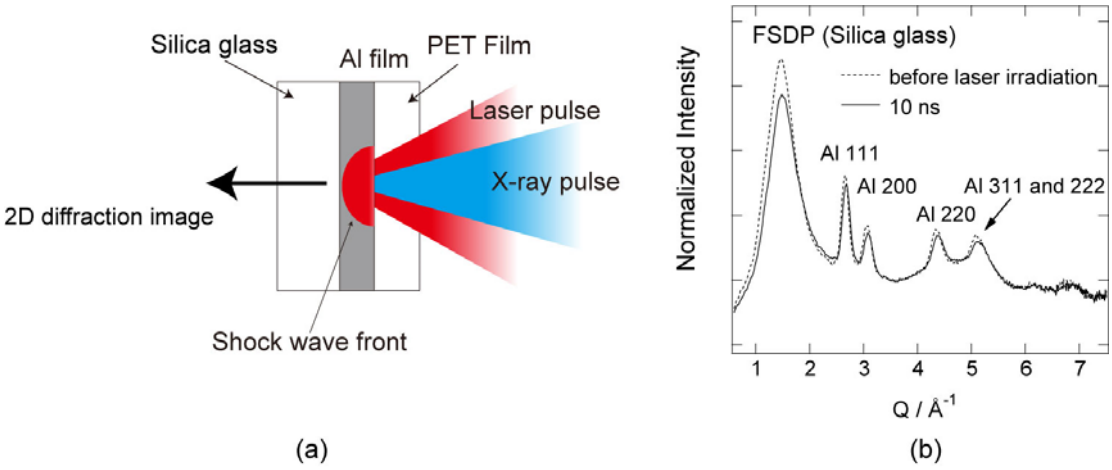

Figure 8. (**a**) Schematic drawing of the plasma confined target of silica glass and a typical X-ray scattering pattern using a single X-ray pulse. Aluminum was an ablator and pressure marker to estimate the shock pressure of silica glass. (**b**) X-ray scattering patterns before laser irradiation (dashed line) and at Δt = 10 ns (solid line). The FSDP of silica glass and X-ray diffraction peaks of aluminum 111, 200, 220, 311, and 222 of the face-centered cubic structure [17] are indicated in the figure. Reproduced with permission from [Applied Physics Letters]. Copyright [2012], AIP Publishing LLC.

Figure 9 shows differential scattering curves for each delay time, with the reference curve before laser irradiation subtracted from the curve for each delay time. After laser ablation, the shock wave generated at the aluminum-PET film interface propagated into the aluminum film. The maximum 111 and 200 peak shifts of aluminum are at $\Delta t \approx 0$ ns, and the shock wave entered the silica glass through the aluminum-silica glass interface. The FSDP shifts to the high Q side. The intermediate-range structure changed with shock wave loading and the pressure release process. At $\Delta t \approx 10$ ns, the shock wave reached and reflected at the free-surface of silica glass. For $\Delta t > 13$ ns, the shock pressure gradually released. These shifts and intensity changes were also seen in hydrostatic compressed silica glass using a synchrotron X-ray source. The intermediate range structure, such as the Si–O–Si bond angle, only changed under shock wave loading in the nonlinear elastic shock region. This time-resolved X-ray scattering method using a short X-ray pulse is able to reveal amorphous structure dynamics under laser-induced shock wave loading.

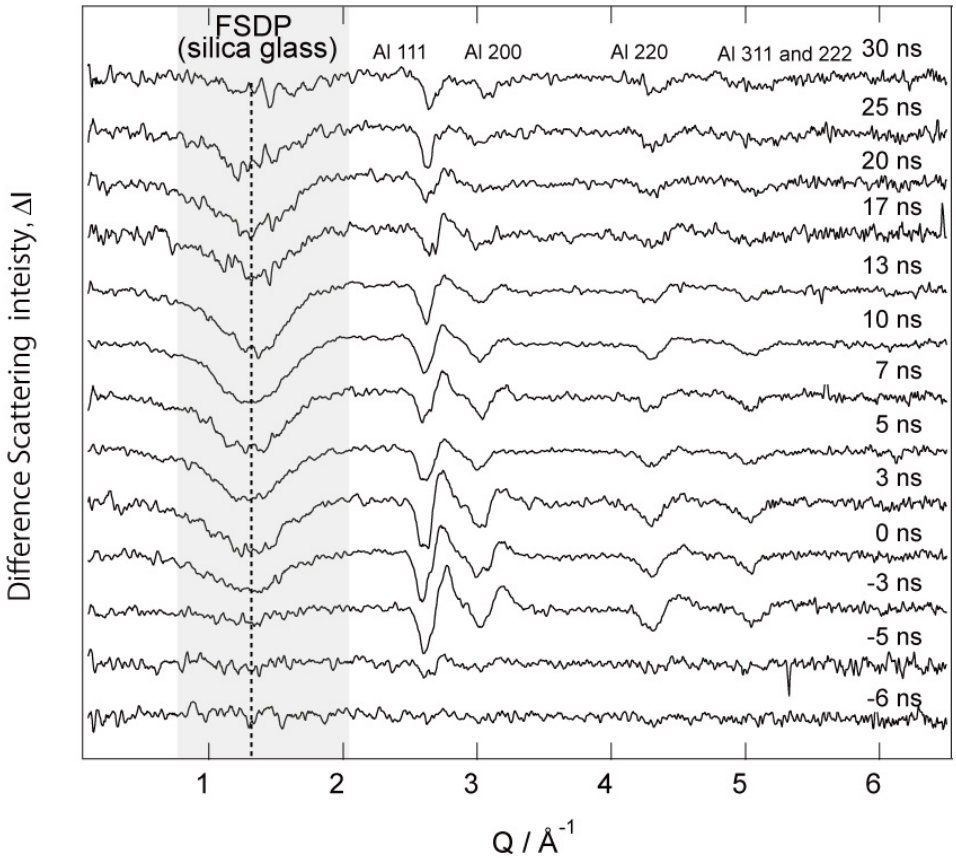

Figure 9. Difference X-ray scattering intensity ΔI as a function of Q at different delay times. The reference curve before laser irradiation was subtracted for each delay time. The gray area is the FSDP of silica glass, which is associated with the intermediate-range structure of glass. The shock wave generated on the aluminum surface occurred at $\Delta t \approx -5$ ns, and propagated into the silica glass at $\Delta t \approx 0$ ns. The shock pressure was released to the ambient pressure at $\Delta t \approx 30$ ns [17]. Reproduced with permission from [Applied Physics Letters]. Copyright [2012], AIP Publishing LLC.

4. Conclusions

Using 100-ps X-ray pulses of synchrotron radiation at the PF-AR (NW-14A beamline) with the laser-shock compression technique, the dynamics of the structural changes of solid materials under non-equilibrium high-pressure conditions were investigated with picosecond time-resolved X-ray diffraction. The present technique can monitor the dynamics of monocrystalline, polycrystalline and glass samples. In a single crystal of CdS, we found that the wurtzite-rocksalt phase transition requires an incubation time of greater than 10 ns, and the over-compressed structure forms before the transition at 3.92 GPa. In a polycrystalline sample of 3Y-TPZ ceramic, the reversible phase transition between tetragonal and monoclinic phases occurs within 20 ns under laser-induced compression and release processes at a peak pressure of 9.8 GPa. In polycrystalline bismuth, a sudden transition from the Bi-I to the Bi-V phase occurs within ~5 ns during the compression process at 11 GPa, and sequential V–III–II–I transitions occurs within 30 ns in the pressure release process. In fused silica shocked at 3.5 GPa, an intermediate-order structural change in the nonlinear elastic region was observed. The phase transitions were observed in polycrystalline samples but not in a single crystal sample within several tens of nanoseconds, which indicates that a large crystal sample requires longer shock duration for the phase transition to occur.

The sequential observation using time-resolved X-ray diffraction is a very powerful technique for monitoring the structural change in many types of materials (from glass to single crystals) under

non-equilibrium high-pressure conditions. Further experiments at much higher pressures, which can be generated with the high-power laser system, are required to study the dynamics of phase transitions in metals and minerals in connection with geoscience and planetary science. The dynamics at much shorter time scale (<picoseconds) will be also studied by using time-resolved X-ray diffraction with high-power laser facility and much shorter and strong pulses from XFEL [13–15] and small-size crystals such as nanocrystals.

Acknowledgments: The authors thank Shunsuke Nozawa, Tokushi Sato, and Shin-ichi Adacchi of KEK, Nobuaki Kawai of Kumamoto University, Jianbo Hu, Katsura Norimatsu, Shinya Kosihara of TokyoTech for their experimental help and valuable discussion about the experiments presented in this review.

Author Contributions: Both co-authors contributed to writing this review article. In particular, K.I. to Sections 1, 2.2, 3.1, 3.4 and 4 and K.G.N. to Sections 1, 2.1, 3.2, 3.3 and 4.

Conflicts of Interest: The authors declare no conflict of interest.

References

1. *Directing Matter and Energy: Five Challenges for Science and the Imagination, A Report from the Basic Energy Science Advisory Committee*; U.S. Department of Energy: Washington, D.C., USA, 2007.
2. Graham, R.A. *Solids under High-Pressure Shock Compression*; Springer-Verlag: New York, NY, USA, 1993; pp. 15–138.
3. Wark, J.S.; Riley, D.; Woolsey, N.C.; Keihn, G.; Whitlock, R.R. Direct measurements of compressive and tensile strain during shock breakout by use of subnanosecond X-ray diffraction. *J. Appl. Phys.* **1990**, *68*, 4531–4534. [CrossRef]
4. Kalantar, D.H.; Chandler, E.A.; Colvin, J.D.; Lee, R.; Remington, B.A.; Weber, S.V.; Hauer, A.; Wark, J.S.; Loveridge, A.; Failor, B.H.; *et al*. Transient X-ray diffraction used to diagnose shock compresses Si crystals on the Nova laser. *Rev. Sci. Instrum.* **1999**, *70*, 629–632.
5. Hironaka, Y.; Yazaki, A.; Saito, F.; Nakamura, K.G.; Takenaka, H.; Yoshida, M. Evolving shock-wave profiles measured in a silicon crystal by picosecond time-resolved X-ray diffraction. *Appl. Phys. Lett.* **2000**, *77*, 1967–1969. [CrossRef]
6. Johnson, Q.; Mitchell, A.C. First X-ray diffraction evidence for a phase transition during shock-wave compression. *Phys. Rev. Lett.* **1972**, *29*, 1369–1371. [CrossRef]
7. Wark, J.S.; Whitelock, R.R.; Hauer, A.; Swain, J.E.; Solone, P.J. Shock launching in silicon studied with use of pulsed X-ray diffraction. *Phys. Rev. B* **1987**, *35*, 9391–9394. [CrossRef]
8. Wark, J.S.; Whitelock, R.R.; Hauer, A.; Swain, J.E.; Solone, P.J. Subnanosecond X-ray diffraction from laser-shocked crystals. *Phys. Rev. B* **1989**, *40*, 5705–5714. [CrossRef]
9. D'Almeida, T.; Gupta, Y.M. Real-time X-ray diffraction measurements of the phase transition in KCl shocked along [100]. *Phys. Rev. Lett.* **2000**, *85*, 330–333. [CrossRef] [PubMed]
10. Podurets, A.M.; Dorokhin, V.V.; Trunin, R.F. X-ray diffraction study of shock-induced phase transformations in zirconium and bismuth. *High Temp.* **2003**, *41*, 216–220. [CrossRef]
11. Kalantar, D.H.; Belak, J.F.; Collins, G.W.; Colvin, J.D.; Davies, H.M.; Eggert, J.H.; Germann, T.C.; Hawreliak, J.; Holian, B.L.; Kadau, K.; *et al*. Direct observation of the α–ε transition in shock-compressed iron via nanosecond X-ray diffraction. *Phys. Rev. Lett.* **2005**, *95*, 075502:1–075502:4.
12. Rygg, J.R.; Eggert, J.H.; Lazicki, A.E.; Coppari, F.; Hawreliak, J.A.; Hicks, D.G.; Smith, R.F.; Socrce, C.M.; Uphaus, T.M.; Yaakobi, B.; *et al*. Powder diffraction from solids in the terapascal regime. *Rev. Sci. Instrum.* **2012**, *83*, 113904:1–113904:7.
13. Gorman, M.G.; Briggs, R.; McBride, E.E.; Higginbotham, A.; Arnold, B.; Eggert, J.H.; Fratanduro, D.E.; Galtier, E.; Lazicki, A.E.; Lee, H.J.; *et al*. Direct observation of melting in shock-compressed bismuth with femtosecond X-ray diffraction. *Phys. Rev. Lett.* **2015**, *115*, 095701:1–095701:5.
14. Nagler, B.; Arnold, B.; Bouchard, G.; Boyce, R.F.; Boyce, R.M.; Callen, A.; Campell, M.; Curiel, R.; Galtier, E.; Garofoli, J.; *et al*. The matter in extreme conditions instrument at the linac coherent light source. *J. Synchrotron Radiat.* **2015**, *22*, 520–525. [PubMed]

15. Schroppe, A.; Hoppe, R.; Meier, V.; Patommel, J.; Seiboth, F.; Ping, Y.; Hicks, D.G.; Beckwith, M.A.; Collins, G.W.; Higginbotham, A.; *et al*. Imaging shock waves in diamond with both high temporal and spatial resolution at an XFEL. *Sci. Rep.* **2015**. [CrossRef]
16. Ichiyanagi, K.; Adachi, S.; Hironaka, Y.; Nakamura, K.G.; Sato, T.; Tomita, A.; Koshihara, S. Shock-induced lattice deformation of CdS single crystal by nanosecond time-resolved Laue diffraction. *Appl. Phys. Lett.* **2007**, *91*, 231918:1–231918:3. [CrossRef]
17. Ichiyanagi, K.; Kawai, N.; Nozawa, S.; Sato, T.; Tomita, A.; Hoshino, M.; Nakamura, K.G.; Adachi, S.; Sasaki, Y.C. Shock-induced intermediate-range structural change of SiO_2 glass in the nonlinear elastic region. *Appl. Phys. Lett.* **2012**, *101*, 181901:1–181901:4. [CrossRef]
18. Hu, J.; Ichiyanagi, K.; Takahashi, H.; Koguchi, H.; Akasaka, T.; Kawai, N.; Nozawa, S.; Sato, T.; Sasaki, Y.; Adachi, S.; *et al*. Reversible phase transition in laser-shocked 3Y-TZP ceramics observed via nanosecond time-resolved X-ray diffraction. *J. Appl. Phys.* **2012**, *111*, 053526:1–053526:5, Erratum, *J. Appl. Phys.* 2013, *113*, 039901:1.
19. Hu, J.; Ichiyanagi, K.; Doki, T.; Goto, A.; Eda, T.; Norimatsu, K.; Harada, S.; Horiuchi, D.; Kabasawa, Y.; Hayashi, S.; *et al*. Complex structural dynamics of bismuth under laser-driven compression. *Appl. Phys. Lett.* **2013**, *103*, 161904:1–161904:5.
20. Bridgman, P.W. Effects of high shearing stress combined with high hydrostatic pressure. *Phys. Rev.* **1935**, *48*, 825–847. [CrossRef]
21. Bridgman, P.W. Shearing phenomena at high pressure of possible importance for geology. *J. Geol.* **1936**, *44*, 653–669. [CrossRef]
22. Ahrens, T.J. Application of shock compression science to earth and planetary physics. In *Shock Compression of Condensed Matter 1995*; AIP Conference Proceedings No. 370; American Institute of Physics: Melville, NY, USA, 1995; pp. 3–8.
23. Jayaraman, A. Diamond anvil cell and high-pressure physical investigations. *Rev. Mod. Phys.* **1983**, *55*, 65–108. [CrossRef]
24. Loubetre, P.; Occelli, F.; LeToullec, R. Optical studies of solid hydrogen to 320 GPa and evidence for black hydrogen. *Nature* **2002**, *416*, 613–617. [CrossRef] [PubMed]
25. Jones, A.H.; Isbel, W.M.; Maiden, C.J. Measurement of the very-high-pressure properties of materials using a light-gas gun. *J. Appl. Phys.* **1966**, *37*, 3493–3499. [CrossRef]
26. Holmes, N.C.; Moriarty, J.A.; Gathers, G.R.; Nellis, W.J. The equation of state of platinum to 660 GPa (6.6 Mbar). *J. Appl. Phys.* **1989**, *66*, 2962–2967. [CrossRef]
27. Moritoh, T.; Kawai, N.; Nakamura, K.G.; Kondo, K. Optimization of a compact two-stage light-gas gun aiming at a velocity of 9 km/s. *Rev. Sci. Instrum.* **2001**, *72*, 4270–4272. [CrossRef]
28. Yokoo, M.; Nkamura, K.G.; Kondo, K.; Tange, Y.; Tuchiya, T. Ultrahigh-pressure scales for gold and platinum at pressures up to 550 GPa. *Phys. Rev. B* **2009**, *80*, 104114:1–104114:9. [CrossRef]
29. Lee, I.-Y.S.; Hill, J.R.; Suzuki, H.; Dolott, D.D.; Baer, B.J.; Chronister, E.L. Molecular dynamics observed 60 ps behind a solid-state shock front. *J. Chem. Phys.* **1995**, *103*, 8313–8321. [CrossRef]
30. Wakabayashi, K.; Nakamura, K.G.; Kondo, K.; Yoshida, M. Time-resolved Raman spectroscopy of polytetrafluoroethylene under laser driven shock compression. *Appl. Phys. Lett.* **1999**, *75*, 947–949. [CrossRef]
31. Matsuda, A.; Nakamura, K.G.; Kondo, K. Time-resolved Raman spectroscopy of benzene and cyclohexane under laser-driven shock compression. *Phys. Rev. B* **2002**, *65*, 174116:1–174116:4. [CrossRef]
32. Matsuda, A.; Kondo, K.; Nakamura, K.G. Nanosecond rapid freezing of benzene under shock compression studied by coherent anti-Stokes Raman spectroscopy. *J. Chem. Phys.* **2006**, *124*, 054501:1–054501:4. [CrossRef] [PubMed]
33. Sato, A.; Oguchi, S.; Nakamura, K.G. Temperature measurement of carbon tetrachloride under laser shock compression using nanosecond time-resolved Raman spectroscopy. *Chem. Phys. Lett.* **2007**, *445*, 28–31. [CrossRef]
34. Cauble, R.; Phillion, D.W.; Hoover, T.J.; Holmes, N.C.; Kilkenny, J.D.; Lee, R.W. Demonstration of 0.75 Gbar planar shocks in X-ray driven colliding foils. *Phys. Rev. Lett.* **1992**, *70*, 2102–2105.
35. Batani, D.; Balducci, A.; Beretta, D.; Bernarinello, A.; Löwer, T.; Koenig, M.; Benuzzi, A.; Faral, B.; Hall, T. Equation of sate data for gold in the pressure range <10 TPa. *Phys. Rev. B* **2000**, *61*, 9287–9294.

36. Wakabayashi, K.; Hattori, S.; Tange, T.; Fujimoto, Y.; Yoshida, M.; Kozu, N.; Tanaka, K.A.; Ozaki, N.; Sasatani, Y.; Takenaka, H.; *et al*. Laser-induced shock compression of tantalum to 1.7 TPa. *Jpn. J. Appl. Phys.* **2000**, *39*, 1815–1816.
37. Nagao, H.; Nakamura, K.G.; Kondo, K.; Ono, T.; Takamatsu, K.; Ozaki, N.; Tanaka, K.A.; Nagai, K.; Nakai, M.; Wakabayashi, K.; *et al*. Hugonipt measurement of diamond under shock compression up to 3 TPa. *Phys. Plasma* **2006**, *13*, 052705:1–052705:5.
38. Cottet, F.; Hallouin, M.; Romain, J.P.; Fabbro, R.; Faral, B.; Pepin, H. Enhancement of a laser-driven shock wave up to 10 TPa by the impedance-match technique. *Appl. Phys. Lett.* **1985**, *47*, 678–680. [CrossRef]
39. Trainor, R.J.; Shaner, J.W.; Auerbach, J.M.; Holmes, N.C. Ultrahigh-pressure laser-driven shock-wave experiments in aluminum. *Phys. Rev. Lett.* **1979**, *42*, 1154–1157. [CrossRef]
40. Benuzzi, A.; Löwer, T.; Koenig, M.; Faral, B.; Batani, D.; Berretta, D.; Danson, C.; Pepler, D. Indirect and direct laser driven shock waves and applications to copper equation of state measurements in the 10–40 Mbar pressure range. *Phys. Rev. E* **1996**, *54*, 2162–2165. [CrossRef]
41. Devaux, D.; Fabbro, R.; Tollier, L.; Bartnicki, E. Generation of shock waves by laser-induced plasma in confined geometry. *J. Appl. Phys.* **1993**, *74*, 2268–2273. [CrossRef]
42. Nozawa, S.; Adachi, S.; Takahashi, J.; Tazaki, R.; Guérin, L.; Daimon, M.; Tomita, A.; Sato, T.; Chollet, M.; Collet, E.; *et al*. Developing 100 ps-resolved X-ray structural analysis capabilities on beamline NW14A at the Photon Factory Advanced Ring. *J. Synchrotron Radiat.* **2007**, *14*, 313–319. [PubMed]
43. Ichiyanagi, K.; Sato, T.; Nozawa, S.; Kim, K.H.; Lee, J.H.; Choi, J.; Tomita, A.; Ichikawa, H.; Adachi, S.; Koshihara, S. 100 ps time-resolve solution scattering utilizing a wide-bandwidth X-ray beam from multilayer optics. *J. Synchrotron Radiat.* **2009**, *16*, 391–394. [CrossRef] [PubMed]
44. Knudsson, M.D.; Gupta, Y.M.; Kunz, A.B. Transformation mechanism for the pressure-induced phase transition in shocked CdS. *Phys. Rev. B* **1999**, *59*, 11704–11715. [CrossRef]
45. Knudsson, M.D.; Gupta, Y.M. Transformation kinetics for the shock wave induced phase transition in cadmium sulfide crystals. *J. Appl. Phys.* **2002**, *91*, 9561–9571. [CrossRef]
46. Tang, Z.P.; Gupta, Y.M. Shock-induced phase transformation in cadmium sulfide in an elastomer. *J. Appl. Phys.* **1988**, *64*, 1827–1837. [CrossRef]
47. Tang, Z.P.; Gupta, Y.M. Phase transition in cadmium sulfide single crystals shocked along *c* axis. *J. Appl. Phys.* **1997**, *81*, 7203–7212. [CrossRef]
48. Bringa, E.M.; Rosolankova, K.; Rudd, R.E.; Remington, B.A.; Wark, J.S.; Duchaineau, M.; Kalantar, D.H.; Hawreliak, J.; Belak, J. Shock deformation of face-centered-cubic metals on subnanosecond timescales. *Nat. Mater.* **2006**, *5*, 805–809. [CrossRef] [PubMed]
49. Garvie, R.C.; Hannink, R.H.; Pascoe, R.T. Ceramic steel? *Nature* **1975**, *258*, 703–704. [CrossRef]
50. Alzyab, B.; Perry, C.H.; Ingel, R.P. High-pressure phase transitions in zirconia and yttria-doped zirconia. *J. Am. Ceram. Soc.* **1987**, *70*, 760–765. [CrossRef]
51. Ohtaka, O.; Kumi, S.; Ito, E. Synthesis and phase stability of cotunnite-type zirconia. *J. Am. Ceram. Soc.* **1988**, *71*, C448–C449. [CrossRef]
52. Igarashi, Y.; Matsuda, A.; Akiyoshi, A.; Kondo, K.; Nakamura, K.G.; Niwase, K. Laser-shock compression of an yttria-doped tetragonal zirconia studied by Raman spectroscopy. *J. Mater. Sci.* **2004**, *39*, 4371–4372. [CrossRef]
53. Yu, E.; Ponyatovsky, E.G. *Phase Transformations of Elements under High Pressure*; CRC: Boca Raton, FL, USA, 2005; p. 148.
54. Pélissier, J.L.; Wetta, N. A model-potential approach for bismuth (I). Densification and melting curve calculation. *Physica A* **2001**, *289*, 459–478.
55. McMahon, M.I.; Degtyareva, O.; Nelmes, R.J. Ba-IV-type incommensurate crystal structure in group-V metals. *Phys. Rev. Lett.* **2000**, *85*, 4896–4899. [CrossRef] [PubMed]
56. McMahon, M.I.; Degtyareva, O.; Nelmes, R.J.; van Smaalen, S.; Palatinus, L. Incommensurate modulations of Bi-III and Sb-II. *Phys. Rev. B* **2007**, *75*, 184114:1–184114:5. [CrossRef]
57. Inamura, Y.; Katayama, Y.; Utsumi, W.; Funakoshi, K. Transformation in the intermediate-range structure of SiO_2 glass under high pressure and temperature. *Phys. Rev. Lett.* **2004**, *93*, 015501:1–015501:4. [CrossRef]
58. Alexander, C.S.; Chhabildas, L.C.; Reinhart, W.D.; Templeton, D.W. Changes to the shock response of fused quartz due to glass modification. *Int. J. Impact Eng.* **2008**, *35*, 1376–1385. [CrossRef]

59. Gibbons, R.V.; Ahrens, T.H. Shock metamorphism of silicate glasses. *J. Geophys. Res.* **1971**, *76*, 5489–5498. [CrossRef]
60. Michell, A.C.; Nelis, W.J. Shock compression of aluminum, copper, and tantalum. *J. Appl. Phys.* **1970**, *52*, 3363–3374. [CrossRef]
61. Barker, L.M.; Hollenbach, R.E. Shock-wave studies of PMMA, fused silica, and sapphire. *J. Appl. Phys.* **1970**, *41*, 4208–4226. [CrossRef]